

## SECONDARY MAXIMUM IN THE NEAR-INFRARED LIGHTCURVES OF TYPE IA SUPERNOVAE

DANIEL KASEN<sup>1,2</sup>

*Draft version October 8, 2018*

### ABSTRACT

We undertake a theoretical study of the near-infrared (NIR) lightcurves of Type Ia supernovae (SNe Ia). In these bands, the lightcurves are distinguished by a secondary maximum occurring roughly 20 to 30 days after the initial one. Using time-dependent multi-group radiative transfer calculations, we calculate the UBVRIJHK-band lightcurves of model SN Ia ejecta structures. Our synthetic NIR lightcurves show distinct secondary maxima, and provide favorable fits to observed SNe Ia. We offer a detailed explanation of the origin of the NIR secondary maximum, which is shown to relate directly to the ionization evolution of iron group elements in the ejecta. This understanding provides immediate intuition into the dependence of the NIR lightcurves on the physical properties of the ejecta, and in particular explains why brighter supernovae have a later and more prominent secondary maximum. We demonstrate the dependence of the NIR lightcurves on the mass of <sup>56</sup>Ni, the degree of <sup>56</sup>Ni mixing, the mass of electron capture elements, the progenitor metallicity, and the abundance of intermediate mass elements (especially calcium). The secondary maximum is shown to be a valuable diagnostic of these important physical parameters. The models further confirm that SNe Ia should be excellent standard candles in the NIR, with a dispersion  $\lesssim 0.2$  mag even when the physical properties of the ejecta are varied widely. This study emphasizes the consummate value of NIR observations in probing the structure of SNe Ia and in furthering their cosmological utility.

*Subject headings:* radiative transfer – supernovae: general

### 1. INTRODUCTION

The extensive monitoring of Type Ia supernovae (SNe Ia) has typically focused on optical band observations, with only occasional ventures into the infrared (Kirshner et al. 1973; Elias et al. 1981, 1985). The situation is now beginning to change, and near-infrared (NIR) observations over the two or three months following explosion are becoming more common, at least for the more nearby events. About a dozen SNe Ia have published, well observed JHK-band lightcurves (e.g., Meikle 2000; Hernandez et al. 2000; Valentini et al. 2003; Candia et al. 2003; Krisciunas et al. 2001, 2003, 2004b,c). NIR spectra have been obtained for several objects as well (Meikle et al. 1996; Bowers et al. 1997; Rudy et al. 2002; Höflich et al. 2002; Marion et al. 2003). Future SN Ia surveys promise to gather NIR lightcurves for a statistically interesting sample of events. With the broadening of our wavelength horizons comes the potential to probe the nature of SN Ia explosions in new ways.

Observational studies of SNe Ia in the NIR have often emphasized their cosmological utility (Krisciunas et al. 2004a). Normal SNe Ia are found to be excellent *standard* (as opposed to calibrated) candles in the NIR, with an intrinsic dispersion of less than 0.2 mag in the J, H, and K bands (Elias et al. 1985; Meikle 2000). Moreover, dust extinction is smaller by a factor  $\sim 5$  in the NIR as compared to the V band, largely eliminating uncertainties in the reddening corrections. The primary challenge for the cosmology studies, naturally, is that SNe Ia are much fainter and harder to observe in the NIR.

The NIR lightcurves of SNe Ia possess a morphology

distinct from those at optical wavelengths. The I through K-band lightcurves are distinguished by the presence of a secondary maximum, occurring roughly 20 to 30 days after the initial one. A corresponding “shoulder” can often be seen also in the R and V-band lightcurves. When the light from all bands is suitably integrated, the bolometric lightcurves sometimes show an inflection at these times as well (Contardo et al. 2000).

In the I-band, the properties of the secondary maximum are found to correlate with the lightcurve decline rate (and hence peak luminosity) of the supernova, being more prominent and occurring later in the broader/brighter SNe Ia (Hamuy et al. 1996b; Nobili et al. 2005). Very subluminous objects may lack a secondary maximum entirely. Similar trends appear in the J, H, and K band lightcurves, although there are interesting exceptions to the rule (Krisciunas et al. 2001; Candia et al. 2003).

Occasional theoretical studies have touched upon the NIR lightcurves of SNe Ia. Höflich et al. (1995) computed I-band and NIR lightcurves for several delayed-detonation models, many of which displayed secondary maxima. The authors explained the double-peaked behavior as a “temperature-radius” effect, in which the expansion of the photosphere compensates for the declining temperature in the ejecta. Wheeler et al. (1998) and Höflich et al. (2002) have further demonstrated the value of NIR spectra in diagnosing the physical conditions in the ejecta. Pinto & Eastman (2000) described the NIR secondary maximum as the release of pre-existing, trapped radiative energy due to a sudden decrease in the flux mean opacity. They placed special emphasis on the role played by stable iron group elements at the ejecta center in this process. Most significantly, Pinto & Eastman (2000) recognized the importance of the ionization state of the ejecta, in particular the in-

<sup>1</sup> Allan C. Davis Fellow, Department of Physics and Astronomy, Johns Hopkins University, Baltimore, MD 21218

<sup>2</sup> Space Telescope Science Institute, Baltimore, MD 21218

creased NIR emissivity of singly as opposed to double ionized iron group elements. This last idea is confirmed and extended in the models studied here.

Despite the theoretical insights, the origin of the NIR secondary maximum and its dependence on the SN ejecta properties have remained in many ways, and to many people, obscure. Moreover, theoretical models of SNe Ia have often had difficulty in fitting the distinctive double-peaked I-band lightcurves (e.g., Hoefflich & Khokhlov 1996; Pinto & Eastman 2000; Blinnikov & Sorokina 2004) whereas very few NIR lightcurve calculations have been attempted (c.f. Hoefflich et al. 1995). This paper focuses exclusively on theoretical models of the far-red and NIR lightcurves of SNe Ia. We calculate the synthetic lightcurves of parameterized ejecta configuration using the time-dependent multi-dimensional radiative transfer code SEDONA (§3). Our model lightcurves show distinct secondary maxima and provide reasonable fits to the observed R, I, J and (to a lesser extent) H and K band lightcurves of SNe Ia (§4).

Close examination of our model calculations provides a clear-cut explanation for the NIR secondary maximum in SNe Ia (§5). The double-peaked behavior is related directly to the ionization evolution of iron group elements in the SN ejecta. In particular, the NIR emissivity of iron/cobalt increases sharply at a temperature  $T \approx 7000$  K marking the transition between the singly and doubly ionized states. The eventual cooling of the iron-rich layers of ejecta to this temperature is thus accompanied by a sudden increase in emission at far red and NIR wavelengths.

Understanding the origin of the secondary maximum provides immediate intuition into the dependence of the NIR lightcurves on the ejecta properties, and allows for theoretical explanations for the empirically established correlations (§6). In particular we study the effect of variations in the mass of  $^{56}\text{Ni}$ , the degree of mixing of  $^{56}\text{Ni}$ , the mass of electron capture elements, the progenitor metallicity, and the abundance of intermediate mass elements (especially calcium). All effects are confirmed with illustrative theoretical models. The NIR secondary maximum is shown to be a valuable diagnostic of these important physical parameters. The models further demonstrate that SNe Ia are indeed excellent standard candles in the NIR, even when the physical properties of the ejecta are varied widely (§7).

## 2. THE NEAR-IR EMISSION OF SNE IA

Before turning to the lightcurve models, we consider the source of NIR emission in SN Ia atmospheres. The luminosity of a SN Ia is powered entirely by the decay of radioactive isotopes synthesized in the explosion, in particular  $^{56}\text{Ni}$  in the decay chain  $^{56}\text{Ni} \rightarrow ^{56}\text{Co} \rightarrow ^{56}\text{Fe}$ . The energetic products of the decay (primarily gamma-rays) heat the SN ejecta, which radiate thermally. The bulk of the radiation occurs initially at ultraviolet (UV) and blue wavelengths. Direct emission at NIR wavelengths (from bound-free and free-free sources) is typically of minor significance.

A portion of the blue/UV radiation pervading the SN ejecta is degraded to red and NIR wavelengths by interaction with lines. The primary redistribution mechanism is fluorescence (Hoefflich 1995; Pinto & Eastman 2000) whereby a UV photon excites a high-energy atomic

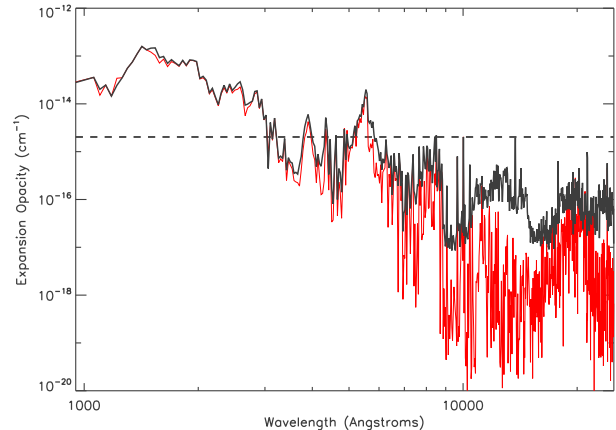


FIG. 1.— Opacity as a function of wavelength of a parcel of cobalt/iron rich ejecta gas at density  $\rho = 10^{-14} \text{ cm}^{-3}$ , temperature  $T = 15000$  K and time since explosion  $t_{\text{exp}} = 20$  days. The composition is 75%  $^{56}\text{Co}$ , 24% iron and 1%  $^{56}\text{Ni}$ . LTE level populations are assumed. The thick black line shows the bound-bound expansion opacity (Equation 1) calculated using the Kurucz CD1 atomic linelist ( $\sim 42$  million lines), while the thin red line is that calculated using the Kurucz CD1 linelist ( $\sim 500,000$  lines). Note the large differences in the near-IR. The horizontal dashed line marks the electron scattering opacity level.

transition, then de-excites via a cascade of longer wavelength transitions (the reverse process is also possible and occurs as well; Mazzali & Lucy 1993). The wavelength redistribution of radiation in atomic lines is responsible for virtually all of the NIR emission observed from SNe Ia. The high velocity gradient in the ejecta Doppler broadens the radiation from each individual transition, and the radiation from literally millions of lines blurs together to form a pseudo-continuum emission in the NIR.

We can calculate, in an approximate way, the NIR opacity and emissivity due to the large complex of lines. A convenient way to capture the average effect is through an expansion opacity formalism (Karp et al. 1977; Eastman & Pinto 1993), in which individual lines are summed together to form a pseudo-continuum opacity

$$\alpha_{\text{exp}}(\lambda) = \frac{1}{ct_{\text{exp}}} \frac{\lambda}{\Delta\lambda} \sum_i (1 - e^{-\tau_i}), \quad (1)$$

where  $t_{\text{exp}}$  is the time since explosion. The sum runs over all lines in the wavelength bin of size  $\Delta\lambda$  at wavelength  $\lambda$ . The quantity  $\tau_i$  is the line Sobolev optical depth (Mihalas 1978).

In Figure 1, we show the expansion opacity calculated for a parcel of iron/cobalt rich ejecta gas at density  $\rho = 10^{-13} \text{ cm}^{-3}$ , temperature  $T = 15000$  K and time  $t_{\text{exp}} = 20$  days, typical of the inner layers of SNe Ia. We use the Kurucz CD1 atomic linelist containing  $\sim 42$  million lines, and compute the atomic level populations assuming local thermodynamic equilibrium (LTE). The iron group expansion opacity increases sharply towards the blue, due to the much larger number of iron group lines occurring at shorter wavelengths.

In Figure 1, we also compare the expansion opacity computed using the much smaller (but commonly applied) Kurucz CD 23 linelist, containing only  $\sim$

500,000 lines. Although the two lists give similar results in the blue, order of magnitude differences appear in the NIR. This emphasizes the large number ( $\sim 5$  million) of relatively weak lines that may contribute to the NIR emission of SNe Ia.

Assuming LTE, the monochromatic emissivity  $\eta_\lambda$  is given by the opacity  $\alpha_{\text{exp}}$  times the blackbody function  $B_\lambda(T)$ . Because we are ultimately interested in the total NIR emission over a broadband wavelength region, we define an average emissivity per gram (units ergs/s/g/Å) over the broadband filter  $F$  by convolving the monochromatic emissivity with the appropriate filter transmission function  $\phi_F(\lambda)$

$$\bar{\eta}_F(T) = \frac{1}{\rho} \frac{\int_0^\infty d\lambda \phi_F(\lambda) B(T, \lambda) \alpha_{\text{exp}}(T, \lambda)}{\int_0^\infty d\lambda \phi_F(\lambda)}. \quad (2)$$

Although this expression formally represents a thermal emission source, under certain conditions it well approximates the operative line fluorescence process as well. In the limit that the time-scales for radiative transitions are short compared other time-scales of interest, the radiation field in the lines approaches the thermodynamic limit embodied by the Planck function. These are the conditions that drive the line source function and level populations close to that of LTE, and should hold approximately at least for the complex iron group species in the deeper layers of ejecta (Baron et al. 1996). Given the dominance of the radiative rates, the temperature  $T$  appearing in Equation 2 should be considered more representative of the radiation field, rather than the electron gas. However, the weak coupling through bound-free and free-free processes may bring the gas and radiation into equilibrium as well (Pinto & Eastman 2000).

Note that, even assuming LTE, the wavelength dependence of the emissivity is not a smooth blackbody function, but depends upon the the number of lines with substantial opacity in a given part of the spectrum. As a result, the NIR emissivity shows a very interesting non-linear dependence upon temperature. In Figure 2, we see that the mean I-band emissivity ( $\bar{\eta}_I$ ) of iron/cobalt-rich gas peaks sharply at temperatures where the gas is near an ionization edge. The most prominent peak is at a temperature  $T_{21} \approx 7000$  K, marking the transition between the singly and doubly ionized states (hereafter termed the  $2 \rightarrow 1$  ionization edge or front).

The interesting dependence of the NIR emissivity on temperature has a simple explanation in terms of the atomic physics. NIR radiation arises from transitions between relatively closely spaced atomic energy levels. The atomic levels are generally more closely spaced at high excitation energy (i.e. high atomic number  $n$ ). Thus, for a given ionization state, the NIR emission increases with temperature as the excited levels become increasingly populated. When the temperature becomes hot enough to ionize the species, however, the NIR emissivity drops rapidly. The ionized species has a higher overall energy scale (being more tightly bound) and hence its excited levels are not highly populated. If the temperature is increased further, this behavior is repeated until the next ionization stage is reached. We emphasize that this emissivity dependence has nothing to do with the energy released from recombination itself, which makes a negligible contribution to the overall energy budget.

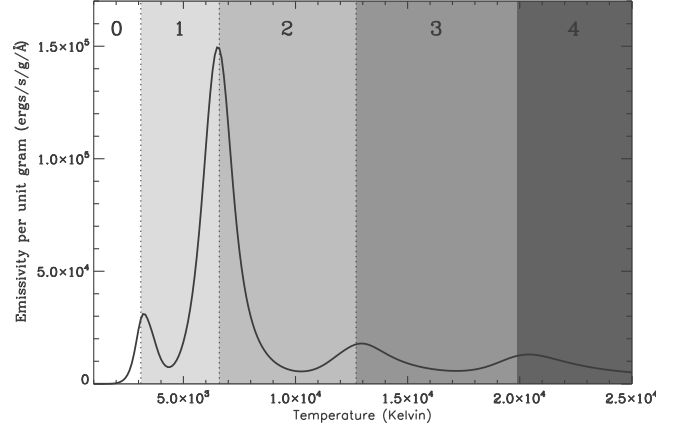


FIG. 2.— Mean I-band emissivity (as a function of temperature) for the iron/cobalt gas discussed in Figure 1 at density  $\rho = 10^{-14}$  cm $^{-3}$  and time since explosion  $t_{\text{exp}} = 40$  days. Calculations use Equation 2, the Kurucz CD1 atomic linelist, and the Bessell (1990) I-band filter profile. The shading illustrates the ionization fraction of the gas, which changes very sharply with temperature at the edges marked in the figure. A strong peak in emissivity is seen at the transition between the singly and doubly ionized states ( $2 \rightarrow 1$ ) occurring at  $T \approx 7000$  K.

For completeness, Figure 3 shows the emissivity for several wavelength bands and for compositions of pure iron, pure cobalt, and a mixture of silicon and sulfur. The emissivity of the iron-group species is qualitatively similar in all NIR bands. A peak at  $T_{21} = 7000$  K occurs also in the optical B and V bands, although it is much less prominent than in the NIR. The relative size of the emissivity peaks depends upon the details of atomic structure, and thus varies somewhat between iron and cobalt and in the different wavelength regions. In general, the iron-group emissivity exceeds that of intermediate mass elements such as silicon and sulfur, except at very high temperatures. This is because the complex iron group valence electron structure leads to a extremely large number of line transitions.

The emissivity behavior shown in Figure 2 turns out to be the key to understanding the NIR secondary maximum in SNe Ia. When the iron rich layers of SN ejecta begin cooling to  $T_{21} \approx 7000$  (which occurs roughly 35 to 40 days after the explosion) the gas becomes very effective in redistributing the blue/UV radiation to longer wavelengths. This leads to the rebrightening of the NIR lightcurves. During these phases, one expects the NIR emission to be dominated by the relatively thin shell of material located near the ionization front at  $T_{21}$ . As the ejecta progressively cools, this shell recedes deeper into the ejecta, following the inward propagation of the  $2 \rightarrow 1$  recombination.

The secondary maximum in the NIR lightcurves is thus identified with the onset and recession of the  $2 \rightarrow 1$  ionization front into iron-rich ejecta. In the next few sections we delineate the process in detail, and show how it serves as an interesting probe of the SN ejecta structure.

### 3. THEORETICAL SNE IA LIGHTCURVE MODELS

A short time after the explosion of a SN Ia ( $\sim 1$  minute) hydrodynamic and nucleosynthetic processes

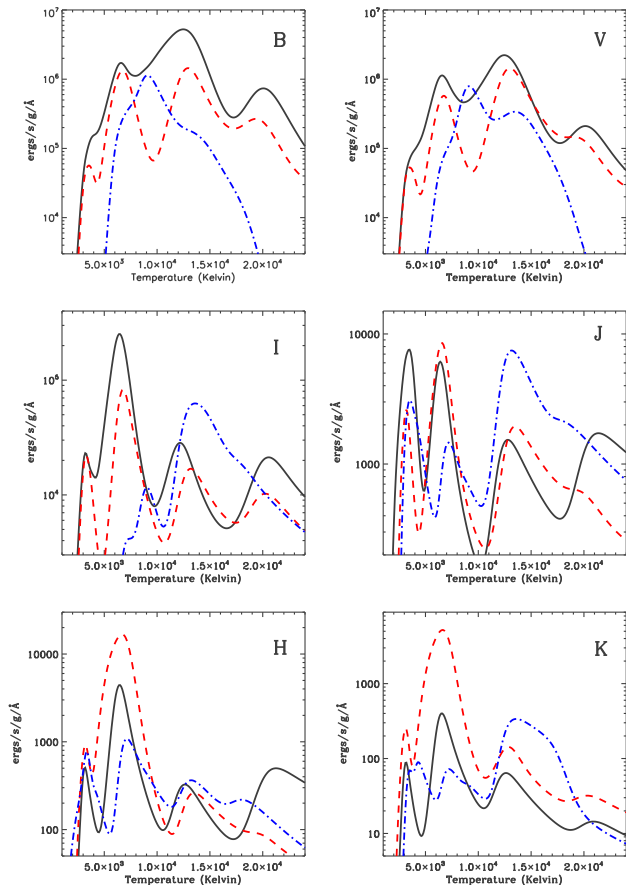


FIG. 3.— A more complete plot of the mean NIR emissivity demonstrated in Figure 2, this time shown for each of the BVIJHK bands and for three compositions: pure iron (solid black), pure cobalt (dashed red) and a mix of 70% silicon and 30% sulfur (dot-dashed blue). The density is  $\rho = 10^{-14} \text{ cm}^{-3}$  and the time since explosion  $t_{\text{exp}} = 40$  days.

abate and the ejected material reaches a phase of nearly free expansion. Thereafter, the essential theoretical challenge becomes to simulate the production and diffusion of photons through the hot and optically thick ejecta – i.e., the radiative transfer problem. Here we calculate broadband model lightcurves by solving the transfer equation using the multi-dimensional time-dependent Monte Carlo code *SEDONA* (Kasen et al. 2006).

### 3.1. Model Ejecta Structures

To demonstrate the basic dependencies of the NIR lightcurves, we calculate synthetic *SEDONA* lightcurves for simple, hand-constructed SN Ia ejecta models. In the free-expansion phase, the velocity of the ejecta is homologous and everywhere proportional to radius:  $r = vt_{\text{exp}}$  where  $t_{\text{exp}}$  is the time since explosion. Given the self-similar nature of the flow, velocity is used as the spatial coordinate in the simulation.

Polarization observations of SNe Ia demonstrate that the asymmetry of the ejecta is typically not large (Wang et al. 2003). We therefore only consider spherically symmetric ejecta structures in this paper. Deviations from sphericity will not effect the basic radiative transfer effects identified here, though they will lead to

some orientation dependence of the model lightcurves.

In 1-dimension (1-D) hydrodynamic explosion models of SNe Ia such as W7 (Nomoto et al. 1984), the final ejecta density structure is well characterized by an exponential. We therefore take the density profile of our ejecta models to be

$$\rho(v, t) = \frac{M_{\text{ch}}}{8\pi v_e^3 t^3} \exp(-v/v_e), \quad (3)$$

where  $M_{\text{ch}}$  is the Chandrasekhar mass and the velocity scale  $v_e = 2750 \text{ km s}^{-1}$  is determined by setting the kinetic energy  $KE = 6M_{\text{ch}}v_e^2$  equal to the energy released in burning  $1.25 M_{\odot}$  of the original carbon/oxygen white dwarf (viz.  $1.6 \times 10^{51}$  ergs).

In analogy to well-known 1-D explosion models such as W7, we tailor a four-zone stratified compositional structure. For our fiducial model these zones are, from the center out: (1)  $0.05 M_{\odot}$  of stable iron peak elements (specifically  $^{54}\text{Fe}$  and  $^{58}\text{Ni}$ , typical of electron capture); (2)  $0.6 M_{\odot}$  of radioactive  $^{56}\text{Ni}$ ; (3)  $0.6 M_{\odot}$  of intermediate mass elements (IME) specifically, Si, S, Ar and Ca, in proportion to their solar abundances (4)  $0.15 M_{\odot}$  of unburned carbon-oxygen with solar metallicity.

To smoothly connect these zones, we use a Gaussian function that allows us to control the degree of mixing. For example, mixing between the  $^{56}\text{Ni}$  and IME layers is assumed to occur over a mass range defined by the free parameter  $a_{\text{Ni}}$ . Above the interface between the two zones (mass coordinate  $m_n = M_{\text{Fe}} + M_{\text{Ni}} - a_{\text{Ni}}/2$ ) the nickel abundance is taken to fall off as

$$X_{\text{Ni}} = \exp(-(M - m_n)^2/a_{\text{Ni}}^2), \quad (4)$$

while the IME abundance is  $X_{\text{IME}} = 1 - X_{\text{Ni}}$ . Similar mixing parameters are defined for the iron and  $^{56}\text{Ni}$  interface ( $a_{\text{Fe}}$ ) and the IME and unburned interface ( $a_{\text{IME}}$ ). In our fiducial model we use  $a_{\text{Ni}} = 0.1$ ,  $a_{\text{Fe}} = 0.05$ , and  $a_{\text{IME}} = 0.1$ . In fact, only  $a_{\text{Ni}}$  is of real consequence to the NIR lightcurves (§6.1).

The rough compositional structure described, while only suggestive of detailed explosion models, is quite adequate for our purposes. The NIR lightcurves are not sensitive to the detailed trace abundances, with one important exception – as we discuss in §6.4, small amounts of calcium can potentially affect the I-band, due to the overwhelming strength of the Ca II IR triplet feature. In all other bands, the overriding factor is the amount and distribution of iron-group elements.

### 3.2. Technical Considerations of the Radiative Transfer

Given a homologously expanding SN ejecta structure, the time-dependent *SEDONA* code calculates high resolution synthetic spectra at each day, from day one to several months after the explosion. Broadband lightcurves are then constructed by convolving the spectrum at each time with the appropriate filter transmission functions. We use the filter profiles of Bessell (1990) for the optical bands and those of Persson et al. (1998) for the JHK bands.

*SEDONA* includes a detailed treatment of gamma-ray transfer to determine the instantaneous energy deposition rate from radioactive  $^{56}\text{Ni}$  and  $^{56}\text{Co}$  decay. Radiative heating and cooling rates are evaluated from Monte Carlo estimators, and the temperature structure of the

ejecta determined by iterating the model to thermal equilibrium. The present calculations use 120 radial zones, 100 time points, and 5000 wavelength groups. Resolution tests confirm the adequacy of this gridding for the problem at hand.

Several significant approximations are made in *SEDONA*, notably the employment of LTE level populations and ionization. In addition, bound-bound line transitions are treated using the expansion opacity formalism (Equation 1) and an approximate two-level atom approach to wavelength redistribution. The ratio of absorption to scattering in lines is calibrated from detailed atomic models and is always close to one. Special care, however, is taken for the calcium lines, which are assumed to be pure scattering for the reasons discussed in §6.4. Note that *SEDONA* allows for a direct Monte Carlo treatment of line fluorescence, but due to computational constraints this functionality is not exploited here. See Kasen et al. (2006) for further code description and verification.

In the tenuous atmospheres of SNe Ia, the microscopic conditions assuring the establishment of LTE level populations and ionization (namely, the dominance of collisional rates) are in fact not met. A direct treatment of the non-LTE physics is thus highly desirable. Unfortunately, a solution of the non-LTE rate equations including the  $\gtrsim 5$  million potentially important line transitions challenges the computational capacity of even the most advanced time-independent spectrum codes. In a fully time-dependent light curve calculation, the adoption of LTE at some level appears inevitable. Fortunately, a wide range of theoretical calculations confirm the adequacy of LTE in reproducing the essential spectral and photometric properties of SN Ia models in both the optical and NIR (e.g., Hoflich et al. 1995; Baron et al. 1996; Pinto & Eastman 2000; Wheeler et al. 1998). In particular, the crucial iron-group species responsible for continuum formation have extremely complex atomic structures and numerous closely spaced atomic levels, and may therefore roughly approximate their equilibrium distributions. However, in other atomic species responsible for individual strong line features non-LTE effects may be significant (especially calcium, see §6.4). In addition, because the ionization state of the ejecta is of particular importance to the NIR lightcurves, LTE becomes increasingly suspect at later times ( $t_{\text{exp}} \gtrsim 70$  days), when the non-thermal ionization by radioactive gamma-rays becomes significant (§4).

An additional, perhaps more serious issue for the transfer calculations is the (in)adequacy of the available atomic data. Because NIR emission occurs in millions of relatively weak atomic lines, using a complete and accurate atomic linelist is critical. We have found the commonly applied CD 23 linelist of Kurucz (1993) (which contains nearly 500,000 lines) to be insufficient for calculation of the IJHK-band lightcurves. Upgrading to the Kurucz CD 1 linelist (with  $\sim 42$  million lines), affords significant improvement, however even this list is likely incomplete and/or inaccurate to some degree. The inadequacy of the line data at long wavelengths likely plagues our synthetic NIR lightcurves, as we discuss further in §4.

#### 4. MODEL NIR LIGHTCURVE OF A NORMAL SNE IA

We have calculated the full spectral evolution and broadband lightcurves for our fiducial SN Ia model con-

taining  $0.6 M_{\odot}$  of  $^{56}\text{Ni}$ . Figure 4 compares the model optical and NIR lightcurves to observations of SN 2001el, a photometrically normal SNe Ia with extensive coverage obtained by Krisciunas et al. (2003). The observed lightcurves have been corrected for dust extinction using the estimates  $A_v = 0.57$  (Krisciunas et al. 2003) and  $R_v = 2.88$  (Wang et al. 2003). We select a distance modulus to SN 2001el of  $\mu = 31.4$  in order to align the peak of the observed  $V$ -band lightcurve with that of the model. This improves the visual comparison of the lightcurve shapes. In fact, Krisciunas et al. (2003) estimate a slightly smaller distance of  $31.29 \pm 0.08$  using the width-luminosity relation of Phillips et al. (1999). This suggests that our synthetic lightcurves are perhaps  $\sim 0.1$  mag brighter than the observed, and that a model with slightly lower  $M_{\text{Ni}}$  (e.g.,  $0.55 M_{\odot}$ ) may be more appropriate for SN 2001el.

The characteristic double-peaked morphology is clearly apparent in all our model NIR lightcurves, with a distinct and prominent secondary maximum occurring in the I, J, H, and K-bands. A corresponding “shoulder” is also seen in the R band, and in the bolometric lightcurve as well (Figure 5). On the whole, the model V, R, I and J-band lightcurves do a favorable job of fitting those of SN 2001el, at least for epochs  $t_{\text{exp}} < 60$  days. The models get progressively worse at later times, but this is also when the transfer calculations are expected to be less reliable. In the model I-band lightcurve, the decline from the first maximum is somewhat too rapid and the secondary maximum occurs slightly earlier than in the observations. We note that the prominence and timing of the secondary maximum is quite sensitive to the model parameters (see §6) and also shows wide variation in the observations (Nobili et al. 2005). A thorough exploration of the model parameter space would likely yield an improved fit to SN 2001el, perhaps in the process illuminating its particular physical characteristics. In addition, polarization observations of SN 2001el indicate that the ejecta was not perfectly spherically symmetric (Wang et al. 2003; Kasen et al. 2003), therefore aspherical ejecta structures may need to be considered to exactly account for all of the lightcurve properties.

The model does a poorer job in the H and K bands. In the observations, the H- and K-band lightcurves are relatively flat for roughly twenty days after B-band maximum ( $t_{\text{exp}} = 18$  days), whereas the models, in contrast, show a strong rise to the secondary maximum during these phases. This is because the model underestimates the luminosity of the initial maximum relative to the secondary one. Attempts to improve the H and K fits by varying the model ejecta structure proved unsuccessful.

It is possible that the relatively poor H and K band lightcurve fits relate to an inadequacy of the LTE approximation, or signal a missing ingredient in our model ejecta structures. However, the primary reason is likely the inadequacy of the atomic linelist. We demonstrate the importance of the atomic data by recomputing the lightcurves using the restricted linelist Kurucz CD23 (containing only 500,000 lines) and comparing to those of our standard linelist (Kurucz CD1, with 42 million lines). The differences in the IJHK lightcurves are considerable (Figure 6), especially at early times. This is not surprising, given the large differences noticed in the opacity calculations of Figure 1

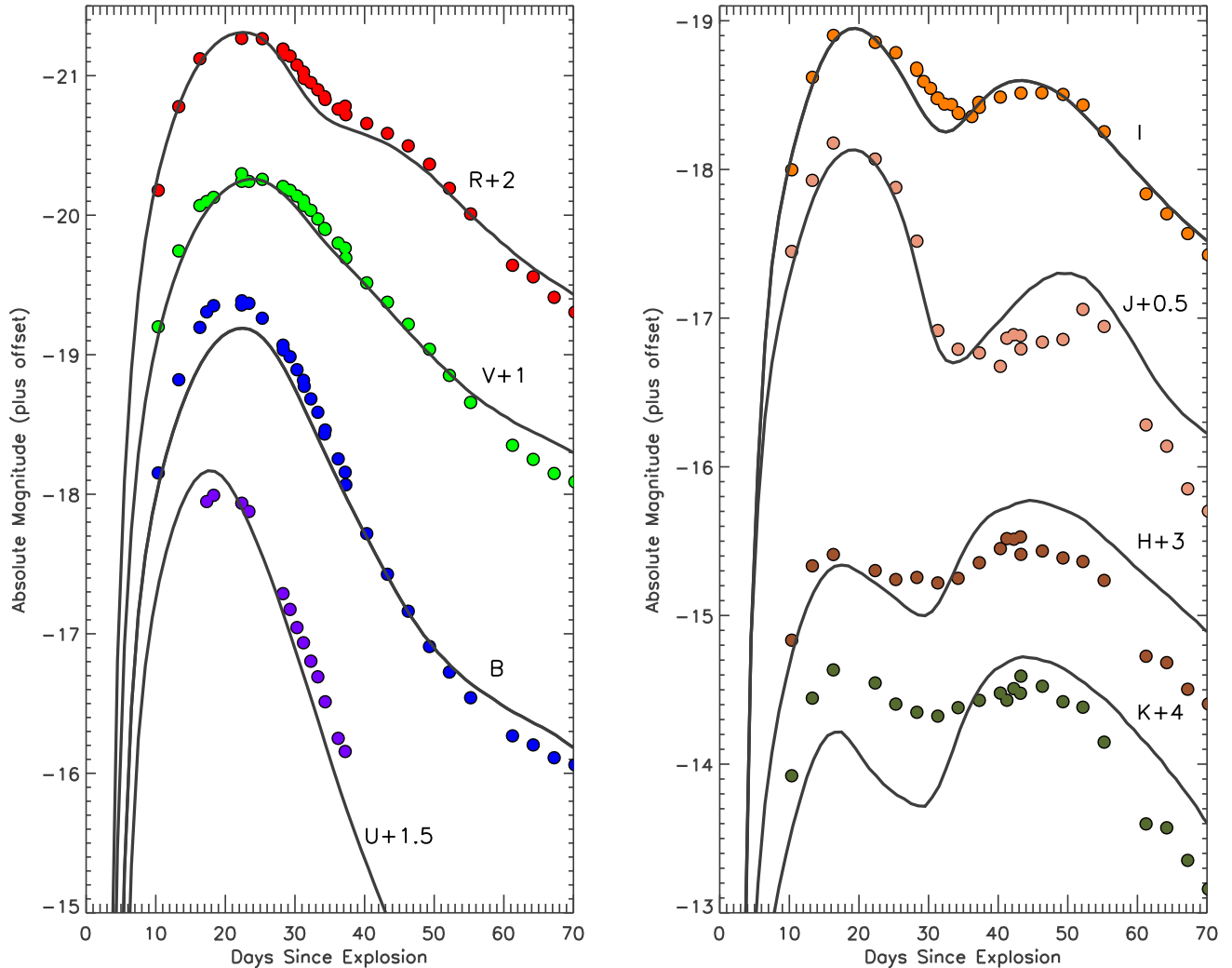


FIG. 4.— Broadband lightcurves of the fiducial model (solid lines) compared to observations of SN 2001el (filled circles).

On the whole, the CD23 IJHK lightcurves do a dramatically poorer job of fitting the observations. In particular, the initial maximum is much too weak in all bands. The problem can be traced directly to the relative lack of higher ionization, longer wavelength iron group lines in the CD23 list. The use of an inadequate linelist may be one reason why previous theoretical models have sometimes had difficulty fitting the I-band lightcurves of SNe Ia. Although CD1 offers significant improvement over CD23, it is natural to suspect that were an even more extensive linelist available, our model *H* and *K* band lightcurves might show significant improvement.

Although not the focus of this paper, we also present NIR spectra of the fiducial model at a few different epochs in Figure 7. Near maximum light, the NIR spectrum is quite featureless, with the occurrence of only a few weak line features from intermediate mass elements. At later times, prominent emission features from blended iron-group lines arise near  $1.6$  and  $1.8 \mu$ . The spectra in Figure 7 show the same general features identified in the

model calculations of Wheeler et al. (1998). The reader can look there for a detailed spectroscopic analysis and comparison with observations.

## 5. EXPLANATION OF THE SECONDARY MAXIMUM

In our models, we trace the origin of the secondary maximum directly to the ionization evolution of iron group elements in the ejecta. In particular, as discussed in §2, the NIR emissivity increases sharply at temperature  $T_{21} \approx 7000$  K in iron/cobalt gas, marking the transition between the doubly and singly ionized states (i.e., the  $2 \rightarrow 1$  ionization edge; see Figure 2). For reasons already discussed, the iron-rich gas becomes exceptionally *phosphorescent* at this temperature, and is very effective in redistributing the pervading UV/blue radiation to longer wavelengths.

Because the temperature in the ejecta decreases with radius, the region near the  $2 \rightarrow 1$  ionization front comprises a relative thin shell of material. During the hot, early epochs, this region lies in the far outer layers of ejecta, but as the SN cools overall the ionization front

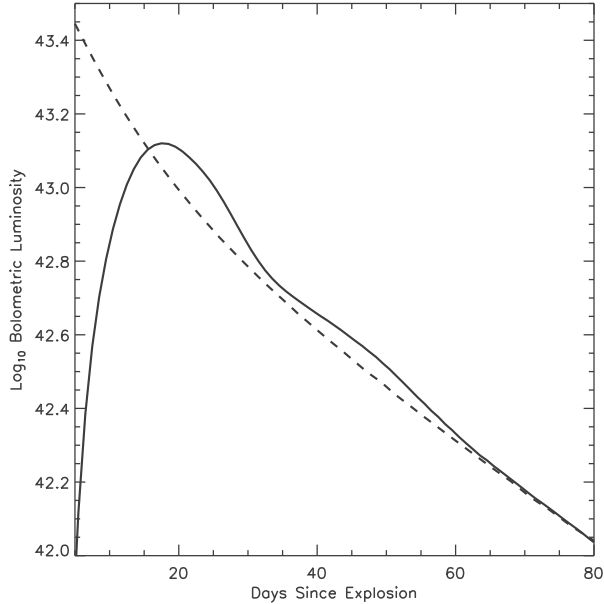


FIG. 5.— Bolometric lightcurve (solid line) and radioactive energy deposition rate (dashed line) for the fiducial model. An inflection in the bolometric lightcurve (corresponding to the NIR secondary maximum) is seen beginning at day 35 after explosion.

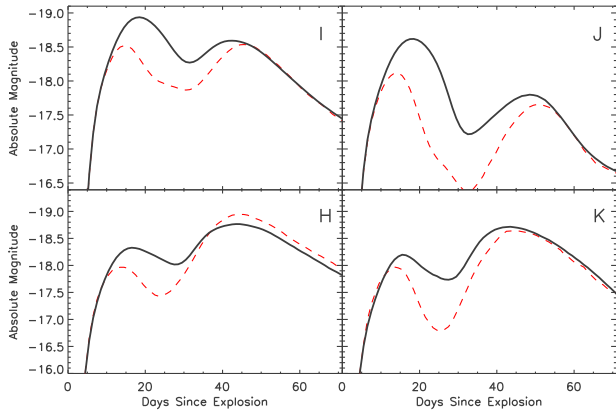


FIG. 6.— Comparison of the IJHK lightcurves of the fiducial model calculated using two different atomic linelists: the 500,000 line Kurucz CD 23 (dashed red lines) and the 42 million line Kurucz CD 1 (solid black lines). Due to the lesser number of lines, the first maximum of the CD23 lightcurves is depressed relative to CD1 in all bands.

recedes deeper (in a Lagrangian sense) into the ejecta. The resulting inward propagating “recombination wave” resembles that often described in models of hydrogen-rich Type IIP supernovae. However, in contrast to the Type IIP’s, the flux mean opacity in SNe Ia does not change substantially over the ionization front and the temperature gradient remains gradual. It is the onset of this recombination wave into the iron-rich core of ejecta that leads to a sudden increase in NIR emission and the re-brightening of the SN in a secondary maximum.

To delineate this process in detail, we examine the evo-

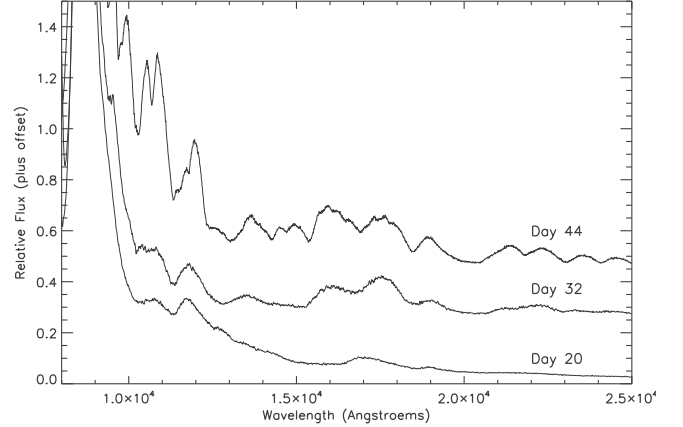


FIG. 7.— Near-infrared spectra of the fiducial SN Ia model at three different epochs. Labels indicate time since explosion.

lution of the NIR emission over time. Figure 8 is a “comic strip” of the spatial distribution of NIR emissivity (in this case, J-band) for the fiducial SN Ia model discussed in the last section. Each panel shows the radial contribution to the J-band emission at a given time, specifically  $d\psi(r) = \eta_J(r)r^2 dr$  where  $r$  is the radius and  $\eta_J$  is the broadband emissivity calculated using Equation 2. This figure is meant mainly as a heuristic – the observed luminosity in the optically thick phases depends not only on the instantaneous emission but also the transfer of radiation through the ejecta.

Given the self-similar nature of the flow, velocity is used as the radial coordinate in Figure 8. The red hatched region identifies the iron-rich core, which extends to roughly  $7000 \text{ km s}^{-1}$  in the model. The green shaded region marks the region near the  $2 \rightarrow 1$  ionization front (specifically, ionization fraction between 1.5 and 1.9). The width of this region, which depends upon the temperature gradient, is typically a few thousand  $\text{km s}^{-1}$ . With time, the ejecta cool and the green shaded region can be seen moving inward, marking the propagation of the  $2 \rightarrow 1$  recombination wave.

We offer a step-by-step discussion of Figure 8. During the early epochs (day 15 after explosion), most of the J-band emission comes from throughout the hot iron core, which has ionization fraction between 3 and 4. Note that the emission is always greatest near the ionization fronts, which are noticed as the emission peaks in the figure. At these early times, the ejecta is optically thick at NIR wavelengths to both electron scattering and bound-bound expansion opacity. The rise time to the first J-band maximum at  $t_{\text{exp}} = 19$  days is thus related to the diffusion time of photons (Arnett 1982).

Following the first J-band maximum, the hot iron core is in the process of recombining from triply to doubly ionized. At these times (days 20 and 25), the NIR emission is dominated by the rather thin shell of material near the  $3 \rightarrow 2$  ionization front. Meanwhile, the  $2 \rightarrow 1$  ionization front forms well outside the iron core and contributes little NIR emission.

By day 30 after explosion, the iron core has nearly completely recombined to doubly ionized and, with the

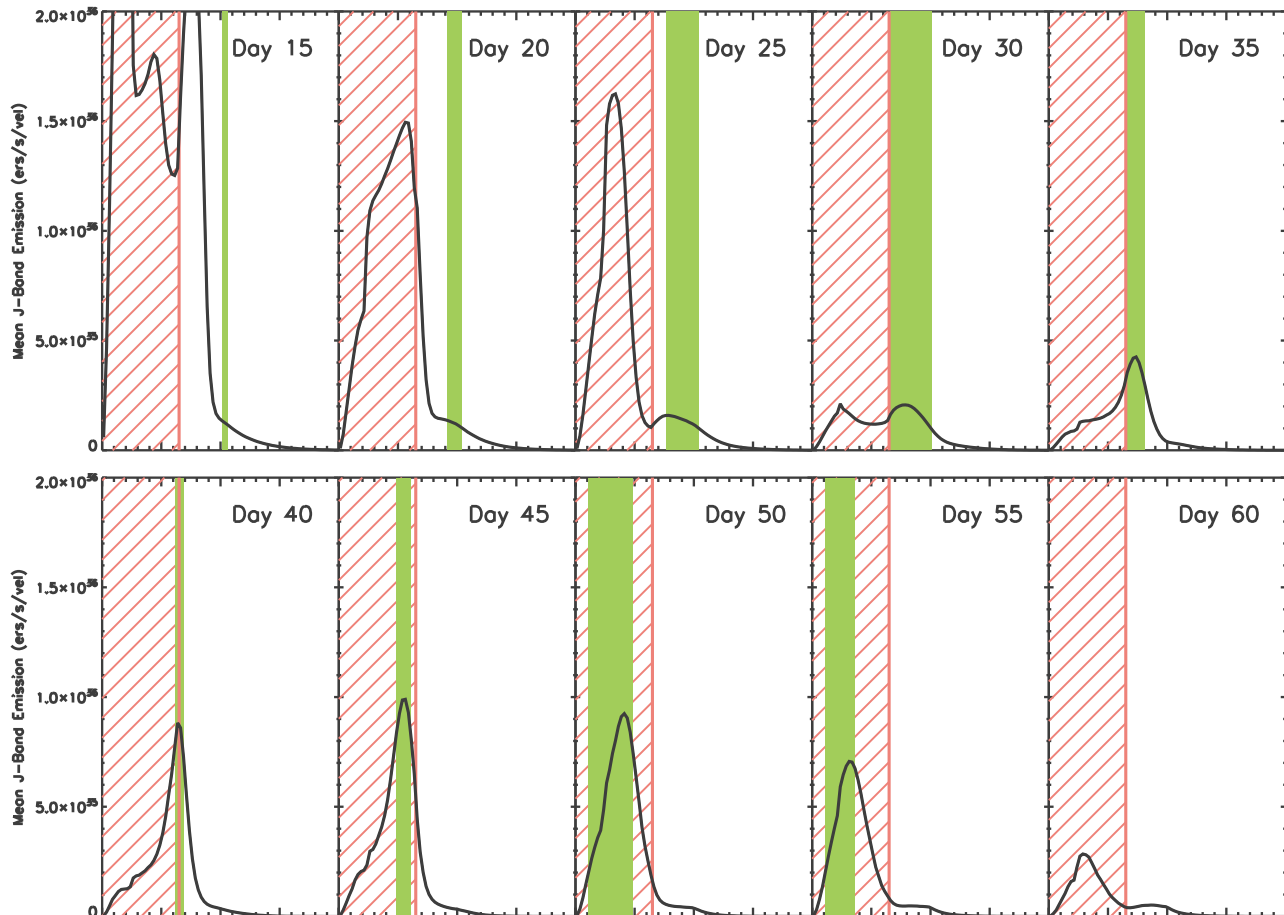


FIG. 8.— Comic strip explaining the origin of the secondary maximum in the NIR lightcurves of SNe Ia. The figure shows the time evolution of the radial distribution of the instantaneous mean J-band emission (solid lines). For each panel, the x-axis is the ejecta velocity coordinate ranging from zero to  $20,000 \text{ km s}^{-1}$ . The red hatched region marks the iron core, which extends to  $v = 7000 \text{ km s}^{-1}$ . The green shaded region marks the region near the  $2 \rightarrow 1$  ionization front. A large spike in J-band emission occurs when that front reaches the iron rich layers of ejecta, leading to the NIR secondary maximum.

passing of the  $3 \rightarrow 2$  ionization front, the NIR emissivity has decreased significantly. This is the local minimum in the J-band lightcurve. The lightcurve would continue to decrease monotonically if weren't for the impending onset of the  $2 \rightarrow 1$  recombination wave. Already this wave has reached the layers just above the iron core, where a small emission peak is visible.

At day 35 the recombination wave reaches the edge of the iron core, and the NIR emission begins to increase dramatically. This is exactly the time at which the model J-band lightcurve begins to re-brighten. The NIR emission is now dominated by the “fluorescent shell” at the  $2 \rightarrow 1$  ionization front. The ejecta are largely transparent in the NIR and radiation emitted from the shell escapes almost immediately. Over the next two weeks, the fluorescent shell recedes further into the iron core, until, at day 50, it is completely contained in the iron rich region. This marks the peak of the J-band secondary maximum.

At later times, as the fluorescent shell recedes yet deeper in the ejecta, its volume decreases and so does the J-band brightness. By day 60, the  $2 \rightarrow 1$  recombi-

nation wave has completely passed, and the iron core is nearly entirely singly ionized. The NIR emission is low and continues to decline.

Why is a secondary maximum seen strongly in the NIR, but not in the optical lightcurves? During the epochs of the secondary maximum, the ejecta remain optically thick at bluer wavelengths ( $\lambda \lesssim 5000 \text{ \AA}$ ). The onset of the  $2 \rightarrow 1$  recombination of iron group elements further increases the opacity in the optical due to the development of broad blends of Fe II and Co II lines in B and V-bands. Thus optical radiation at the  $2 \rightarrow 1$  ionization front can not immediately escape the ejecta, but continues to diffuse out gradually or to fluoresce to longer wavelengths. Meanwhile, the ejecta are transparent in the NIR, and photons fluorescing to these wavelengths escape straightaway. The net effect of the recombination wave is therefore to redistribute flux from the optical to longer wavelengths.

In Figure 5, we see that at the onset of the secondary maximum (day 35 after explosion) a slight bump also occurs in the model bolometric lightcurve.



This inflection has been noted in observed SNe Ia lightcurves (Contardo et al. 2000) and has been explained by Pinto & Eastman (2000) as the release of pre-existing, trapped radiative energy. The ejecta are optically thick (at bluer wavelengths) for the first couple months after explosion, and the average diffusion time of photons is a significant fraction of the expansion time. A store of trapped radiation continually accumulates in the supernova ejecta. It is the gradual leaking of this energy reservoir that causes the bolometric luminosity to exceed the instantaneous radioactive energy deposition rate from day 18 until full transparency is reached near day 70. At day 35, the onset of the  $2 \rightarrow 1$  ionization front in the iron core suddenly enhances photon escape via fluorescence into the NIR. This opens up a new means of release of the trapped SN radiation, causing a slight rise in the bolometric lightcurve.

As an interesting aside, notice that the NIR emissivity also peaks when the gas recombines from singly ionized to neutral (Figure 2). In principle, the propagation of another recombination wave ( $1 \rightarrow 0$ ), could lead to a *third* bump in the NIR lightcurves. In the current models, a third maximum is in fact seen at  $t_{\text{exp}} \approx 100$  days ( $\sim 80$  days after B-band maximum), most prominently in the *J* band. However, the inadequacies of the LTE approximation at late epochs make this behavior suspect. In particular, the non-thermal ionization from radioactive gamma-rays becomes significant at low temperatures (Swartz 1991) and will keep the ejecta from ever going completely neutral. This may minimize or delay the putative third maximum. In addition, emission by forbidden transitions (not included here) may also become significant at these epochs. Meanwhile, most published SNe Ia observations lack NIR data at times  $> 60$  days after maximum.

## 6. DEPENDENCE ON PHYSICAL PARAMETERS

The above explanation of the NIR secondary maximum provides immediate intuition into the dependence of the NIR lightcurves on the physical properties of the ejecta. This allows for simple explanations of the observed trends concerning the timing and prominence of the secondary maximum.

First, the rise to a secondary maximum occurs when the  $2 \rightarrow 1$  ionization front first reaches the ejecta layers rich in iron group elements. Thus the timing of the secondary maximum will depend upon both the size of the iron core (or more precisely, its velocity extent), and the overall temperature scale of the ejecta. All other things being equal, SNe with larger iron cores can be expected to have earlier secondary maxima. Hotter SNe can be expected to have later ones.

Second, the luminosity of the second maximum depends fundamentally upon the size and luminosity of the fluorescent shell formed when the  $2 \rightarrow 1$  recombination wave has receded into the bulk of the iron core. All other things being equal, SNe Ia with larger iron cores can be expected to have a brighter secondary maximum.

Below we discuss these behaviors in the context of SNe Ia ejecta properties. In particular, we consider the effects of the degree of mixing, the  $^{56}\text{Ni}$  mass, the mass of electron capture elements, the progenitor metallicity, and the mass of intermediate elements produced, demonstrating each of these with the models.

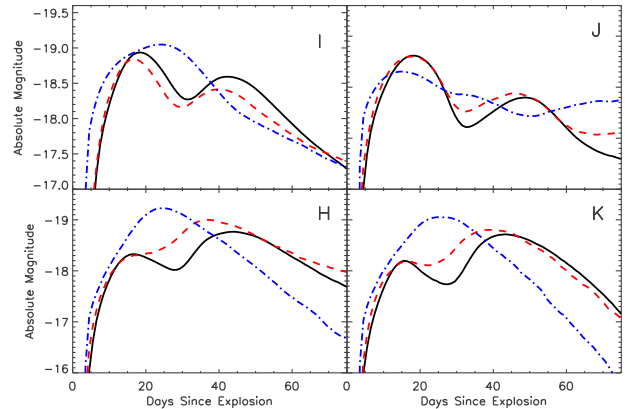


FIG. 9.— Effect of the outward mixing of  $^{56}\text{Ni}$  on the NIR lightcurves. The figure compares the well-stratified fiducial model (mixing parameter  $a_{\text{Ni}} = 0.2$ , solid black lines) to a model with enhanced  $^{56}\text{Ni}$  mixing ( $a_{\text{Ni}} = 0.6$ ; red dashed lines) and a model with a completely homogenized composition structure (blue dot-dashed lines).

### 6.1. Mixing

The fiducial SN Ia model studied in the last section was compositionally stratified, with iron group elements (primarily  $^{56}\text{Ni}$ ) concentrated in the central core. The mixing of  $^{56}\text{Ni}$  outward into the region of IME effectively increases the velocity extent of the iron core. Naturally, we expect this to hasten the occurrence of the NIR secondary maximum.

We demonstrate this effect by comparing the NIR lightcurves of our fiducial model (mixing parameter  $a_{\text{Ni}} = 0.2$ ) to one in which  $^{56}\text{Ni}$  is more thoroughly mixed outward ( $a_{\text{Ni}} = 0.5$ ). The result of the mixing (Figure 9) is to advance the NIR secondary maximum by about 5 days and to decrease its contrast with the first maximum. In the I and J-band lightcurves, the first and second maxima are blended, but still distinguishable. In the H and K band lightcurves the double-peaked structure is nearly lost entirely.

In Figure 9 we show also the lightcurves of a fully mixed model (i.e., the fiducial model with a completely homogenized compositional structure). In this case, the first and second maxima are indistinguishable in every band (except for perhaps a small inflection at day 35 in J). We conclude that the double-peaked structure observed in NIR lightcurves is a direct indication of the abundance stratification in SNe Ia, in particular the concentration of iron-peak elements in the central regions. Thus NIR observations should be useful in constraining the exact degree of mixing in SNe Ia.

### 6.2. Mass of $^{56}\text{Ni}$

The mass of  $^{56}\text{Ni}$  ( $M_{\text{Ni}}$ ) powers the luminosity of SNe Ia and is the primary determinate of the peak brightness of the event.  $M_{\text{Ni}}$  also affects, in part, the B-band lightcurve decline rate (or stretch) and is commonly identified as the fundamental parameter controlling the well-known width-luminosity relation.

In observations, the properties of the I-band secondary maximum are found to correlate with stretch (and hence

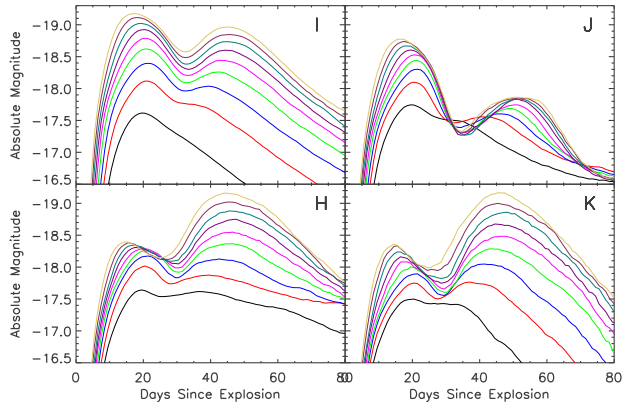


FIG. 10.— Effect of the mass of  $^{56}\text{Ni}$  ( $M_{\text{Ni}}$ ) on the NIR lightcurves. The model lightcurves demonstrate variations in  $M_{\text{Ni}}$  from 0.1 to  $0.9 M_{\odot}$  in  $0.1 M_{\odot}$  increments. The less luminous models are those with lower  $M_{\text{Ni}}$ .

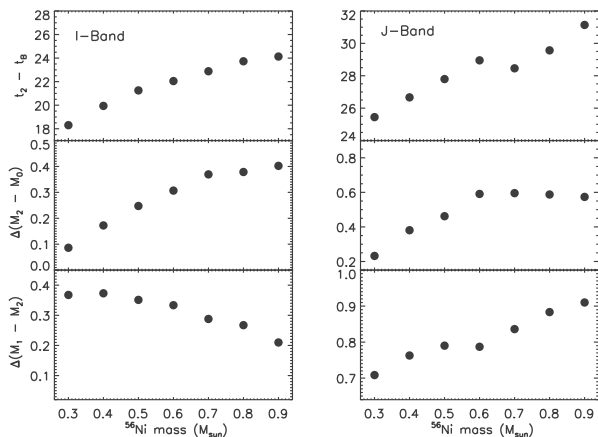


FIG. 11.— Prominence and timing of the secondary maximum versus  $M_{\text{Ni}}$  for the models of Figure 10 in the I-band (left) and J-band (right). *Top panels:* Time (in days) of secondary maximum minus time of first maximum. *Middle panels:* Number of magnitudes that the secondary maximum is brighter than the local minimum that precedes it. *Bottom panels:* Number of magnitudes the first maximum is brighter than the secondary maximum.

peak luminosity), being more prominent and occurring later in the broader/brighter SNe Ia. The origin of these empirical relations can be addressed within the theoretical paradigm we have described. To demonstrate, we construct a series of models (based upon the fiducial model) in which we vary  $M_{\text{Ni}}$  between 0.1 to  $0.9 M_{\odot}$  in increments of  $0.1 M_{\odot}$ . The sum of  $M_{\text{Ni}}$  and the mass of IME is held fixed at  $1.25 M_{\odot}$ , such that all models have roughly equal kinetic energy. All other model parameters have been held fixed.

As in observations, the model secondary maxima are more pronounced in the higher  $M_{\text{Ni}}$  models, disappearing altogether for the lowest  $M_{\text{Ni}}$  models (Figure 10). This is due primarily to the larger size of the iron core in higher  $M_{\text{Ni}}$  models, leading to a larger and more luminous fluo-

rescent shell at the  $2 \rightarrow 1$  ionization front. The observed behavior may therefore be taken as further evidence that more slowly declining SNe Ia have a larger production of iron group elements.

$M_{\text{Ni}}$  produces two opposing effects on the timing of the secondary maximum. A larger  $M_{\text{Ni}}$  leads to higher overall temperatures and thus a later development of the  $2 \rightarrow 1$  recombination wave. This tends to delay the secondary maximum. However, a larger  $M_{\text{Ni}}$  also implies a larger iron core, which would tend hasten the secondary maximum. From Figure 10, we see that the first of these effects dominates, at least for  $M_{\text{Ni}}$  in the range  $0.1 - 0.8 M_{\odot}$ . Thus our models recover the observed timing trend, which should be understood fundamentally as the physical correlation between the supernova’s luminosity and its ionization state.

For the models with low  $M_{\text{Ni}}$ , the secondary maximum occurs at early times and begins merging with the initial maximum. In our most subluminous example ( $M_{\text{Ni}} = 0.1 M_{\odot}$ ) the ejecta are so cool that the  $2 \rightarrow 1$  recombination wave reaches the iron core at  $t_{\text{exp}} \approx 20$  days. For these objects, the secondary maximum is absent, or rather it is coincident with the first.

For reference, Figure 11 quantifies the timing and prominence relations in the I and J bands. We note that the observed trends depend to some extent on how the quantities are empirically defined. In the J-band, for example, the peak magnitude of the secondary maximum increases with  $M_{\text{Ni}}$  relative to the magnitude at the local minimum, but *decreases* relative to the first maximum. This reflects complexities glossed over in our discussion (such as the parameters affecting the initial maximum) and demonstrates the need to compare observations and models in a uniform way. Also keep in mind that additional parameters (described below) can also have profound effects on the secondary maximum, and may play a role in these relations as well.

### 6.3. Electron Capture Elements and Progenitor Metallicity

In addition to  $^{56}\text{Ni}$ , SNe Ia may synthesize substantial amounts of stable iron group elements, in particular  $^{54}\text{Fe}$  and  $^{58}\text{Ni}$ . Although this material does not contribute to the overall luminosity of the SN, it does modify the radial extent of the iron core. Thus we anticipate it having important effects on the timing and prominence of the secondary maximum.

Stable iron group material can be produced by two distinct processes in SN Ia explosions: (1) In standard 1-D explosion models, nuclear burning at the highest densities is subject to electron capture, leading to the synthesis of  $0.5\text{-}2.0 M_{\odot}$  of neutronized stable iron group species at the very center of the ejecta (Nomoto et al. 1984; Thielemann et al. 1986). There is some observational evidence suggesting such a pure stable iron center does exist in SNe Ia (Höflich et al. 2004). (2) While burning to nuclear statistical equilibrium produces primarily  $^{56}\text{Ni}$ , some small fraction of stable iron group may also be produced, depending upon the metallicity of the progenitor white dwarf (Thielemann et al. 1986; Timmes et al. 2003). For solar metallicity, this fraction would be  $\sim 5\%$ , while for metallicity three times solar the fraction may be as high as  $\sim 25\%$ . The stable iron group material arising from the progenitor metallicity would be evenly

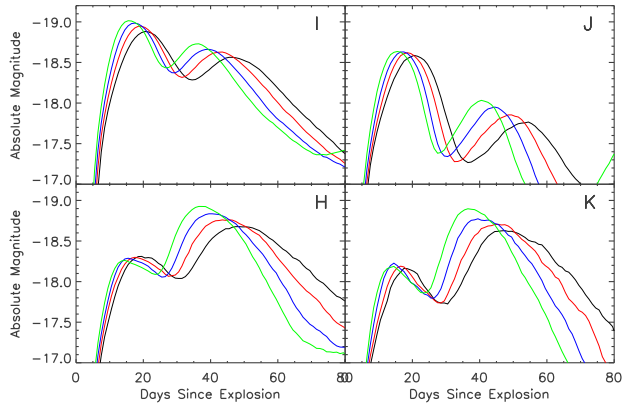


FIG. 12.— Effect of electron capture elements on the NIR lightcurves. The model lightcurves demonstrate variations in the mass of stable iron group elements ( $M_{\text{Fe}}$ ) produced by electron capture at the ejecta center. The models are  $M_{\text{Fe}} = 0.0 M_{\odot}$  (black line),  $M_{\text{Fe}} = 0.1 M_{\odot}$  (red line),  $M_{\text{Fe}} = 0.2 M_{\odot}$  (blue line) and  $M_{\text{Fe}} = 0.3 M_{\odot}$  (green line).

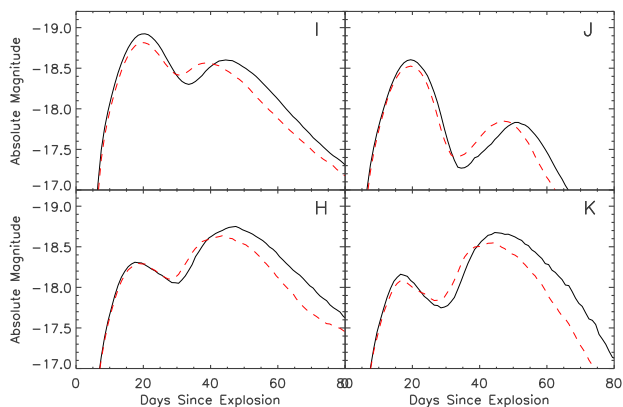


FIG. 13.— Effect of progenitor metallicity on the NIR lightcurves. The black line is the fiducial model with zero stable iron production in the  $^{56}\text{Ni}$  zone (corresponding to near zero metallicity). The dashed red line is the model with 25% stable iron production throughout the  $^{56}\text{Ni}$  zone (corresponding to a metallicity near 3 times solar).

distributed in low abundance throughout the  $^{56}\text{Ni}$  zone.

We demonstrate each of these effects in turn. First, we vary the mass of stable iron group species ( $M_{\text{Fe}}$ ) produced by electron capture at the ejecta center. We explore values of  $M_{\text{Fe}}$  from 0 to  $3.0 M_{\odot}$  while keeping fixed  $M_{\text{Ni}} = 0.6 M_{\odot}$  and the total burned mass  $M_{\text{Fe}} + M_{\text{Ni}} + M_{\text{IME}} = 1.25 M_{\odot}$ . Figure 12 shows the resulting NIR lightcurves. Because the mass of  $^{56}\text{Ni}$  is held fixed, the temperature and ionization evolution is very similar in all these models. However, in models with larger values of  $M_{\text{Fe}}$  (and hence larger iron cores) the  $2 \rightarrow 1$  recombination wave encounters the layers of iron rich material at relatively earlier times. The secondary maximum thus occurs as many as ten days earlier in models with larger  $M_{\text{Fe}}$ . In addition, the peak magnitude of the secondary maximum increases with  $M_{\text{Fe}}$ ,

again due to the larger iron core size.

Pinto & Eastman (2000) have suggested that the stable iron group material at the ejecta center plays a fundamental role in producing the NIR secondary maximum. We note that this is not strictly the case, as a clear secondary maximum occurs even when no stable iron is included in the model.

One finds a similar dependence on the stable iron production due to progenitor metallicity. In Figure 13 we take the fiducial model and vary the abundance of stable  $^{54}\text{Fe}$  throughout the  $^{56}\text{Ni}$  zone from zero to 25%, corresponding to a metallicity variation of roughly zero to 3 times solar. The total mass in the  $^{56}\text{Ni}$  zone is held fixed at  $0.6 M_{\odot}$  – i.e., in this construction stable iron is produced at the expense of  $^{56}\text{Ni}$ . Thus the higher metallicity model has lower bolometric luminosity, lower temperatures, and an earlier onset of the  $2 \rightarrow 1$  recombination wave. The secondary maximum thus occurs about seven days earlier in the higher metallicity model.

Because the size of the iron core remains fixed in the models of Figure 13, one expects the absolute luminosity of the secondary maximum to remain nearly constant. This is indeed the case in the I and J band lightcurves. Interestingly, however, the H and K band secondary maximum are slightly brighter in the low metallicity models. This is due to the significantly larger emissivity of cobalt compared to iron at these wavelengths (see Figure 3). Thus the relative strength of the secondary maxima in different NIR bands may turn out to be a useful measure of the ratio of cobalt to iron in the bulk ejecta, and hence the progenitor metallicity.

Significantly, the effect of stable iron group elements on the NIR lightcurves is distinct from that of  $^{56}\text{Ni}$ . The predicted correlation (i.e., earlier secondary maxima are as bright or brighter than later ones) conflicts with the primary observed trend. Variations in iron group elements is thus one potential source of deviation from the standard NIR lightcurve behavior. This emphasizes the value of NIR observations in providing constraints of the progenitor metallicity and the early explosion processes.

#### 6.4. Calcium Distribution and the IR Triplet Feature

On the whole, the distribution of intermediate mass elements in the ejecta has little direct effect on the NIR lightcurves. Emission from iron group lines dominates the continuum flux, and few individual IME line features are significant. The one exception is in the I-band, where the prominent Ca II IR triplet feature ( $gf$ -weighted rest wavelength  $8579 \text{ \AA}$ ) can potentially affect the photometry significantly. The triplet lines are intrinsically very strong, and may remain optically thick far out in the low density layers of ejecta, even when the calcium abundance is very low ( $X_{\text{Ca}} \approx 0.01$ ).

Unfortunately, the net effect of the Ca II lines on the I-band lightcurve depends upon the details of the radiative transfer, specifically the line source functions. Two limiting cases can be considered: (1) If the calcium lines are assumed to be pure scattering, flux is nearly conserved over the line profile – i.e., the absorption component of the P-Cygni profile nearly cancels the emission component. In this case, the line feature should have only a minor effect on the broadband magnitude. (2) If, on the other hand, the calcium lines are assumed to be completely absorbing (as in pure LTE calculations) the net

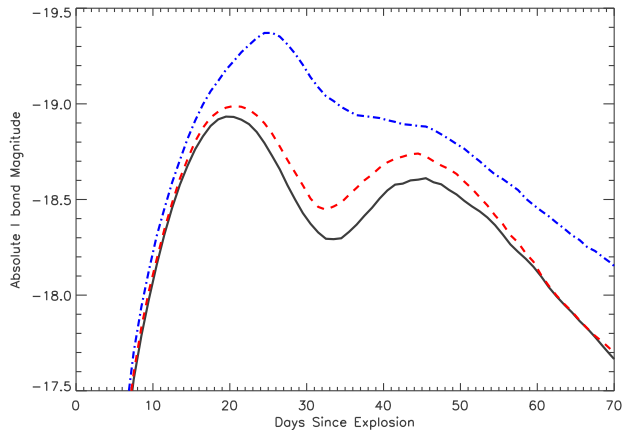


FIG. 14.— Effect of the Ca II IR triplet feature on the I-band lightcurve. For reference, the red dashed line shows the fiducial model lightcurve when all calcium is removed. If the calcium lines are assumed to be pure scattering, the IR triplet feature leads to a modest decrease in the I-band magnitude (solid black line). If the calcium lines are assumed to be pure absorbing, emission in the triplet feature increases the I-band magnitude significantly (blue dot-dashed line).

emission in the Ca II IR triplet feature can be considerable, because radiation absorbed in blue part of the spectrum is allowed to re-emerge in the triplet lines. In the models of this paper we have always assumed pure scattering calcium lines, for the reasons described below.

Figure 14 quantifies the net effect of calcium on the I-band lightcurve by comparing the fiducial model to a similar model in which all calcium has been removed. Under the pure scattering assumption, the Ca II triplet feature causes modest ( $\sim 0.1$  mag) I-band differences. These arise for two reasons. First, because of blending with other lines, flux is not strictly conserved over the triplet line profile. Second, because the Bessell (1990) I-band filter profile cuts off near  $8500 \text{ \AA}$ , the absorption and emission component of the triplet feature are not equally sampled. Thus, under pure scattering, the calcium feature serves to slightly *decrease* the I-band magnitude.

If, on the other hand, the calcium lines are assumed to be pure absorbing, net emission in the triplet features enhances the peak I-band magnitude by  $\sim 0.5$  mag, and delays the time of peak by nearly seven days. The secondary maximum is no longer distinct and prominent, and the model I-band lightcurve does not fit the observed lightcurve shape or colors. The result emphasizes that the I-band secondary maximum does not occur because of emission in the Ca II triplet feature, but rather *in spite* of it.

From an atomic physics perspective, the low collisional rates in the SN ejecta and the large oscillator strength of the Ca II triplet lines suggest that pure scattering is indeed the more plausible representation of the line source functions. This is supported by our lightcurve fits to the SN 2001el observations. To the extent that pure scattering does hold, the shape and peak brightness of the I-band lightcurves of SNe Ia will be generally insensitive (at the  $\lesssim 0.1$  mag level) to the details of calcium produc-

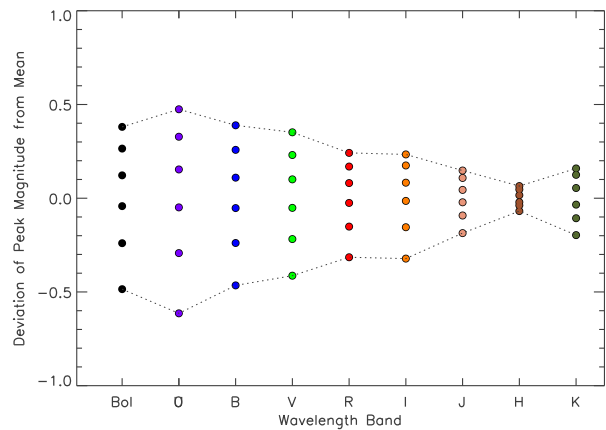


FIG. 15.— Dispersion in peak magnitude (measured at the first lightcurve maximum) as a function of wavelength band for the models of Figure 10 with  $^{56}\text{Ni}$  masses between  $0.4$  and  $0.9 M_{\odot}$ .

tion and distribution. This is an important condition for the robust application of I-band lightcurves to cosmology studies. One interesting exception is worth noting: if the calcium distribution deviates from spherical symmetry, flux scattered in the triplet feature will be redistributed anisotropically along different viewing angles.

The results of this section necessitate the inclusion of a non-LTE treatment of the calcium level populations within the fully time-dependent multi-dimensional radiative transfer calculation. This solution is in fact readily incorporated into the Monte Carlo approach, and will be included in the upcoming version of SEDONA. The common adoption of purely absorbing lines in previous LTE radiative transfer studies may be another reason why those calculations often found difficulty in fitting the I-band lightcurves of SNe Ia.

## 7. NEAR-IR SN IA AS STANDARD CANDLES

The cosmological interest in NIR observations of SNe Ia stems from the small observed dispersion ( $\sim 0.2$  mag) in the peak JHK-band magnitudes. We explore this property here using the models discussed in §6.2 (and shown in Figure 10) for which the mass of  $^{56}\text{Ni}$  is varied. We consider only those models with  $^{56}\text{Ni}$  mass in the “normal” range of  $0.4$  to  $0.9 M_{\odot}$ .

Figure 15 shows the spread in model peak magnitude (measured at the first maximum) as a function of broadband filter. One notices a general decline in the dispersion towards the red. In the B-band, the spread is roughly  $\pm 0.5$  mag, similar to the observed (uncorrected) dispersion (Hamuy et al. 1996a). This decreases to  $\pm 0.4$  mag in V and  $\pm 0.3$  mag in R and I. In the NIR, the dispersion is more than a factor two in magnitude smaller than the B-band, being  $\sim 0.2$  mag in J and K and  $\sim 0.1$  mag in H. For the H and K bands, bear in mind the failure of the models to fix the observed first maximum, presumed an inadequacy of the atomic data. Nevertheless, this level of NIR dispersion is very similar to that inferred from observations (Meikle 2000).

In addition, the model peak NIR magnitudes show an impressive insensitivity to the other physical parameters explored in this paper. Significant variations in

the progenitor metallicity, electron capture elements, and IME production all only led to small ( $\sim 0.1$  mag) variations in the absolute magnitude of the initial peak (Figures 12, 13, and 14). The mixing of  $^{56}\text{Ni}$  also caused only slight magnitude variations unless extreme levels of mixing were considered (Figure 9). These results further testify to the robustness of SNe Ia NIR lightcurves as standard candles.

Our model lightcurves may also suggest further refinements to cosmology studies in the NIR. The J-band lightcurves, for example, show almost *zero* intrinsic dispersion at the local minimum occurring between the first and secondary maximum (about 15 days after B-band maximum; see Figure 10). Even when the subluminous models are considered the magnitude variations at this epoch are small. It would be interesting to check if observed SNe Ia exhibit a similar behavior. As it turns out, Meikle (2000) chose to study the J-band magnitudes of SNe Ia measured 14 days after B-maximum (as derived from fits to the Elias et al. (1985) templates). He found that the dispersion in  $M_{14}(J)$  was small, although not necessarily minimal.

The low peak magnitude dispersion in the NIR follows from the dependence of the model colors on the bolometric luminosity. The dimmer SNe also have lower temperatures, and radiate a greater percentage of the energy at redder wavelengths. This acts as a regulating mechanism which maintains a nearly constant peak magnitude in the NIR bands, regardless of the  $^{56}\text{Ni}$  mass. On the other hand, the dispersion in ultraviolet and *U*-band magnitudes is reciprocally intensified, exceeding that of the bolometric lightcurves.

## 8. DISCUSSION AND CONCLUSION

We have modeled the far-red and NIR lightcurves of SNe Ia and given a detailed explanation of the characteristic secondary maximum. Our synthetic model lightcurves were calculated using parameterized 1-D ejecta configurations and the time-dependent multi-group radiative transfer code SEDONA. The model lightcurves displayed distinct and conspicuous secondary maxima and provided favorable fits to the NIR observations of the normal Type Ia SN 2001el. By varying the mass of  $^{56}\text{Ni}$ , the models also reproduced the observed trend that brighter SNe Ia have later and more prominent secondary maxima.

We trace the origin of the secondary maximum directly to the ionization evolution of iron group elements in the ejecta. Specifically, the NIR emissivity of iron/cobalt gas peaks sharply at a temperature  $T_{21} \approx 7000$  K, marking the transition between the singly and doubly ionized states. The recombination of iron-rich gas from  $2 \rightarrow 1$  thus leads to enhanced redistribution of radiation from blue to NIR. Interestingly, as the supernova cools, the global ionization evolution takes the form a  $2 \rightarrow 1$  “recombination wave” gradually receding deeper into the ejecta. The onset and propagation of this wave through the iron rich layers marks the rise and fall the secondary maximum. Because the ejecta are transparent at longer wavelengths during these epochs, the NIR observations allow us to watch directly as the recombination wave scans progressively through deeper and deeper layers of ejecta.

While the models considered in this paper captured

the essential aspects of SN Ia NIR lightcurves, they also highlighted several outstanding issues for the radiative transfer calculations. First, the use of a complete and accurate atomic linelist proved critical in modeling the NIR bands. Further improvement of the currently available atomic data is likely needed to accurately model the H and K-band lightcurves. Second, non-thermal ionization effects from radioactive gamma-rays become significant for  $t_{\text{exp}} \gtrsim 70$  days when LTE predicts neutrality, and thus likely have a dramatic impact on the NIR lightcurves at these late epochs. Third, a proper treatment of Ca II IR triplet line source function is crucial in synthesizing accurate I-band model lightcurves, as the assumption of purely absorbing lines leads to unrealistic results. Future advances to the SEDONA code will permit more detailed studies of these and other important effects. However, one does not expect the technical developments to change the general NIR lightcurve trends and dependencies explained in this paper.

In this paper, we studied the dependence of the NIR lightcurves on a number of important physical parameters, which highlighted the many ways in which NIR lightcurves offer valuable diagnostics of the ejecta properties and powerful constraints on explosion models.

First, the double-peaked morphology of the NIR lightcurves can be taken as a direct consequence of the abundance stratification in SNe Ia, in particular the concentration of iron group elements in the central regions. This confirms previous inferences based upon post-maximum and nebular spectra (e.g., Branch et al. 1985; Höflich et al. 2002; Kozma et al. 2005). Abundance stratification is generic to certain classes of explosion models, for example the delayed detonation models (Khokhlov 1991) and the detonation from failed detonation (Plewa et al. 2004). In contrast, models characterized by large-scale mixing, such as published 3-dimensional deflagration models (Gamezo et al. 2003; Reinecke et al. 2002) are likely inconsistent with the double peaked behavior in the NIR lightcurves. Further NIR observations, coupled with the transfer models, should be useful in constraining the exact degree of  $^{56}\text{Ni}$  mixing in SNe Ia, and thus in testing current and future explosion paradigms.

Second, the luminosity of the secondary maximum provides a measure of the amount of iron group elements (both stable and radioactive) synthesized in the explosion. The observed correlation between B-band decline rate and the luminosity of the secondary maximum provides strong evidence that slower declining SNe Ia have (on average) a larger production of iron group elements. This conclusion coincides with several other inferences to the same (Contardo et al. 2000; Mazzali et al. 1998; Stritzinger et al. 2006).

Third, the NIR secondary maximum is sensitive to the amount of stable iron group elements produced in the explosion, and hence the progenitor metallicity. Timmes et al. (2003) has suggested that metallicity variations may lead to 25% variations in  $^{56}\text{Ni}$ . We find that the NIR signature of this variation is distinct from that of varying  $^{56}\text{Ni}$  independently. Our predicted correlation arising from metallicity variations is that earlier secondary maxima will be as bright or brighter than later ones. This conflicts with the primary observed trend, and suggests that the metallicity is likely a sub-dominant

cause of SN Ia luminosity variations. This signature further opens the possibility of using an observational sample of NIR lightcurves to constrain metallicity variations among different progenitor populations.

Fourth, the timing of the secondary maximum is a direct probe of the temperature and ionization evolution in the ejecta, and hence a useful tool in interpreting observations. As it turns out, the ionization evolution of crucial importance to the optical lightcurve decline rate as well. The  $2 \rightarrow 1$  recombination of iron group elements contributes significantly to blanketing in the B and V-bands due to the development of blends of strong Fe II and Co II lines in the optical part of the spectrum. In this context, NIR observations may also be especially useful in diagnosing peculiar objects. For example, the paradoxical SN 2002cx was  $\sim 2$  mag subluminous, but had a peculiar spectrum characteristic of “hot” iron-rich ejecta (Li et al. 2003). NIR observations would complement that spectroscopic analyses by providing independent measures of the temperature scale, ionization evolution, iron core size and mixing.

Finally, we reiterate the cosmological utility of the NIR lightcurves of SNe Ia. In our lightcurve models, the dispersion in NIR peak magnitudes is found to be small ( $\lesssim 0.2$  mag) even when the physical properties of the ejecta are varied widely. At certain epochs (e.g., the J-band local minimum occurring near day 15 after B-maximum) the predicted dispersion is even smaller. Our models thus further testify to the robustness of SNe Ia

NIR lightcurves as standard candles.

Perhaps more importantly, the NIR observations provide deep and readily interpreted diagnostics of the physical conditions in the SN Ia ejecta, and therefore offer an opportunity for controlling potential systematic errors in the cosmology studies. We have shown that the physical parameters affecting the NIR secondary maximum are also those that may modulate the optical peak brightness and decline rate of SNe Ia. Thus the NIR lightcurves are one of the most promising places to search for empirical secondary parameters related to deviations from the standard width-luminosity relation.

In this context, the NIR observations strike a nice balance in their level of information content. Given the double-peaked morphology, the NIR lightcurves carry considerably more information than do the single-peaked optical band observations; at the same time, they remain simple enough to submit to a much more ready statistical analysis than do the complex spectral time series. For all these reasons, a sizable sample of observed NIR lightcurves would be a remarkably powerful tool in constraining the possible evolution or progenitor drift of SNe Ia arising in differing stellar populations. This potential should be exploited further with expanded observational programs and concerted theoretical efforts.

The author thanks Kevin Krisciunas and Peter Meikle for helpful comments and suggestions.

#### REFERENCES

- Arnett, W. D. 1982, *ApJ*, 253, 785  
 Baron, E., Hauschildt, P. H., Nugent, P., & Branch, D. 1996, *MNRAS*, 283, 297  
 Bessell, M. S. 1990, *PASP*, 102, 1181  
 Blinnikov, S., & Sorokina, E. 2004, *Ap&SS*, 290, 13  
 Bowers, E. J. C., Meikle, W. P. S., Geballe, T. R., Walton, N. A., Pinto, P. A., Dhillon, V. S., Howell, S. B., & Harrop-Allin, M. K. 1997, *MNRAS*, 290, 663  
 Branch, D., Doggett, J. B., Nomoto, K., & Thielemann, F.-K. 1985, *ApJ*, 294, 619  
 Candia, P. et al. 2003, *PASP*, 115, 277  
 Contardo, G., Leibundgut, B., & Vacca, W. D. 2000, *A&A*, 359, 876  
 Eastman, R. G., & Pinto, P. A. 1993, *ApJ*, 412, 731  
 Elias, J. H., Frogel, J. A., Hackwell, J. A., & Persson, S. E. 1981, *ApJ*, 251, L13  
 Elias, J. H., Matthews, K., Neugebauer, G., & Persson, S. E. 1985, *ApJ*, 296, 379  
 Gamezo, V. N., Khokhlov, A. M., Oran, E. S., Chitchekanova, A. Y., & Rosenberg, R. O. 2003, *Science*, 299, 77  
 Höflich, P., Gerardy, C. L., Fesen, R. A., & Sakai, S. 2002, *ApJ*, 568, 791  
 Hamuy, M., Phillips, M. M., Suntzeff, N. B., Schommer, R. A., Maza, J., & Aviles, R. 1996a, *AJ*, 112  
 Hamuy, M., Phillips, M. M., Suntzeff, N. B., Schommer, R. A., Maza, J., Smith, R. C., Lira, P., & Aviles, R. 1996b, *AJ*, 112, 2438  
 Hernandez, M. et al. 2000, *MNRAS*, 319, 223  
 Höflich, P., & Khokhlov, A. 1996, *ApJ*, 457, 500  
 Hoffich, P. 1995, *ApJ*, 443, 89  
 Höflich, P., Gerardy, C. L., Nomoto, K., Motohara, K., Fesen, R. A., Maeda, K., Ohkubo, T., & Tominaga, N. 2004, *ApJ*, 617, 1258  
 Hoffich, P., Khokhlov, A. M., & Wheeler, J. C. 1995, *ApJ*, 444, 831  
 Karp, A. H., Lasher, G., Chan, K. L., & Salpeter, E. E. 1977, *ApJ*, 214, 161  
 Kasen, D. et al. 2003, *ApJ*, 593, 788  
 Kasen, D., et al. 2006, *ApJ*, submitted  
 Khokhlov, A. 1991, *A&A*, 245, 114  
 Kirshner, R. P., Willner, S. P., Becklin, E. E., Neugebauer, G., & Oke, J. B. 1973, *ApJ*, 180, L97+  
 Kozma, C., Fransson, C., Hillebrandt, W., Travaglio, C., Sollerman, J., Reinecke, M., Röpke, F. K., & Spyromilio, J. 2005, *A&A*, 437, 983  
 Krisciunas, K. et al. 2001, *AJ*, 122, 1616  
 Krisciunas, K., Phillips, M. M., & Suntzeff, N. B. 2004a, *ApJ*, 602, L81  
 Krisciunas, K. et al. 2004b, *AJ*, 127, 1664  
 —. 2003, *AJ*, 125, 166  
 —. 2004c, *AJ*, 128, 3034  
 Kurucz, R. 1993, CD-ROM 1, Atomic Data for Opacity Calculations (Cambridge: Smithsonian Astrophysical Observatory)  
 Li, W. et al. 2003, *PASP*, 115, 453  
 Marion, G. H., Höflich, P., Vacca, W. D., & Wheeler, J. C. 2003, *ApJ*, 591, 316  
 Mazzali, P. A., Cappellaro, E., Danziger, I. J., Turatto, M., & Benetti, S. 1998, *ApJ*, 499, L49  
 Mazzali, P. A., & Lucy, L. B. 1993, *A&A*, 279, 447  
 Meikle, W. P. S. 2000, *MNRAS*, 314, 782  
 Meikle, W. P. S., et al. 1996, *MNRAS*, 281, 263  
 Mihalas, D. 1978, *Stellar Atmospheres* (San Francisco: W. H. Freeman)  
 Nobili, S. et al. 2005, *A&A*, 437, 789  
 Nomoto, K., Thielemann, F., & Yokoi, K. 1984, *ApJ*, 286, 644  
 Persson, S. E., Murphy, D. C., Krzeminski, W., Roth, M., & Rieke, M. J. 1998, *AJ*, 116, 2475  
 Phillips, M. M., Lira, P., Suntzeff, N. B., Schommer, R. A., Hamuy, M., & Maza, J. 1999, *AJ*, 118, 1766  
 Pinto, P. A., & Eastman, R. G. 2000, *ApJ*, 530, 757  
 Plewa, T., Calder, A. C., & Lamb, D. Q. 2004, *ApJ*, 612, L37  
 Reinecke, M., Hillebrandt, W., & Niemeyer, J. C. 2002, *A&A*, 391, 1167  
 Rudy, R. J., Lynch, D. K., Mazuk, S., Venturini, C. C., Puetter, R. C., & Höflich, P. 2002, *ApJ*, 565, 413  
 Stritzinger, M., Leibundgut, B., Walch, S., & Contardo, G. 2006, *A&A*, 450, 241  
 Swartz, D. A. 1991, *ApJ*, 373, 604  
 Thielemann, F.-K., Nomoto, K., & Yokoi, K. 1986, *A&A*, 158, 17  
 Timmes, F. X., Brown, E. F., & Truran, J. W. 2003, *ApJ*, 590, L83  
 Valentini, G. et al. 2003, *ApJ*, 595, 779

- Wang, L. et al. 2003, ApJ, 591, 1110  
Wheeler, J. C., Hoefflich, P., Harkness, R. P., & Spyromilio, J. 1998,  
ApJ, 496, 908